Tracking photoinduced charge separation in a perfluorinated Zn-tetraphenylporphyrin sensitizer

Daniel H Cruz Neto, Philipp Gotico, Thu-Trang Tran, Caroline Szantai, Zakaria Halime, Marie Sircoglou, Juan Soto, Karine Steenkeste, Daniel Peláez, Thomas Pino, et al.

Tracking Photoinduced Charge Separation in a Perfluorinated Zn-Based Tetraphenylporphyrin Sensitizer

Daniel H. Cruz Neto,[a] Philipp Gotico,[b] Thu-Trang Tran,[a] Caroline Szantai,[a] Zakaria Halime,[c] Marie Sircoglou,[c] Juan Soto,[d] Karine Steenkeste,[a] Daniel Peláez,*[a] Thomas Pino,*[a], Minh-Huong Ha-Thi*[a]

[a]*Institut des Sciences Moléculaires d'Orsay (ISMO), CNRS, Université Paris-Saclay, Orsay, France*

[b]*Institute for Integrative Biology of the Cell (I2BC), CEA, CNRS, Université Paris-Saclay, Gif-sur-Yvette, Orsay*

[c]*Institut de Chimie Moléculaire et des Matériaux d'Orsay (ICMMO), CNRS, Université Paris-Saclay, Orsay, France*

[d]*Department of Physical Chemistry, Faculty of Science, University of Málaga, Málaga, Spain*

Abstract: The development of artificial biomimetic systems with real-world applications relies on a profound understanding of all photophysical and photochemical processes taking place upon light absorption by a chromophoric unit. Efficient photoinduced charge separation in photosensitizers or specialized photocatalysts is the process triggering most of the chemical reactions in the production of solar fuels, and so its proper characterization is of utmost importance. In this work, we investigate photoinduced charge separation processes in a perfluorinated Zn-tetraphenylporphyrin photosensitizer (ZnF_{20}). Ascorbate and 1,4-diazabicyclo[2.2.2]octane (DABCO) are used as reversible electron donors for the nanosecond-resolved pump-probe experiments using both optical absorption and resonance Raman scattering as probes. Our results show that, in spite of similar charge separation efficiencies, the DABCO-containing system exhibits a much faster kinetics of the charge-separated state formation and decay . This is attributed to its inherent ability to coordinate to the metal center. Time-resolved resonance Raman measurements allow for the detection of vibrational modes specific to both the triplet excited state of ZnF_{20} and to its reduced state, complementing transient absorption data to fully characterize the charge separation process.

Introduction

The daring promise of artificial photosynthesis, a strategy to mitigate carbon dioxide (CO_2) emissions, heavily relies on the fundamental comprehension of photoinduced charge transfer processes in carefully engineered biomimetic systems capable of both charge separation and accumulation of redox equivalents.[1–5] The very development of the next generation of dedicated materials can only be accomplished by fine-tuning their behavior once submitted to photonic excitations as a way to induce chemical transformations. Achiving this requires a great deal of burdensome spectroscopy-based mechanistic investigations, supported by their theoretical counterparts, to shine some light on the principles that must guide molecular design towards long-lived charge-separated states.[6]

Be as troubling as it may, we now have access to proper experimental tools to interrogate such fundamental processes on a myriad of biomimetic systems that can

be engineered with different strategies. Some of the most well-known approaches employ basic donor-photosensitizer-acceptor (D-PS-A) units, either covalently-constructed[7–9] or in a multicomponent configuration,[10,11] to mimic the photoinduced processes (multiple electron transfers and accumulation) taking place in natural systems. Built on the blueprints of the natural photosynthetic process, such systems take us ever closer to realizing an actual functional biomimetic system that could potentially fullfill the promise of solar fuel production.

As far as the light-absorbing units, photosensitizers, are concerned, prototypical Ru(II) polypyridyl complexes remain unchallenged in terms of photochemical and photophysical properties,[12–16] but porphyrin-based compounds have been gaining attention as reasonable alternatives. Among them, zinc tetraphenylporphyrin (ZnTPP) derivatives not only have been widely used as photosensitizers for different applications[17–22] and in supramolecular self-assemblies,[23–25] but they have even shown photo-[26] and electrocatalytic[27] proton and CO_2 reduction activities, respectively, which makes them an even more valuable class of compounds. Because of these capabilities, they can also be used as photocatalysts for light-induced reduction reactions in artificial photosystems.

On the donor/acceptor side, not only their thermodynamical compatibility with the photosensitizer's excited state has to be taken into account, but implications in the charge separation kinetics are also relevant depending on whether these species are covalently bound or not. Consequently, the complete reversible cycle of reductive/oxidative quenching of the photosensitizer has to be investigated in detail prior to any systematic attempt at using the charge-separated species to trigger chemical transformations of any kind.

It is in this context that we now report the complete characterization of the photoinduced and reversible electron transfer processes taking place in a perfluorinated Zn-tetraphenylporphyrin photosensitizer (hereafter referred to as ZnF_{20}, Figure 1). For this, we use complementary time-resolved probes of optical light absorption and resonance Raman scattering in the standard pump-probe approach. This molecule shows two reversible reductions in CH_3CN (Figure S1), with E_{red} (Zn^{II}/Zn^{I}) = -0.68 V vs. the normal hydrogen electrode (NHE) and E_{red} (Zn^{I}/Zn^{0}) = -1.07 V vs. NHE. The addition of 10% H_2O causes cathodic shifts of 30 and -10 mV, respectively (Figure S1).

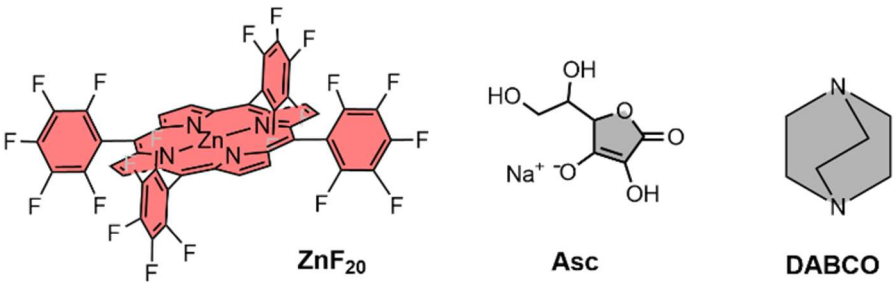

Figure 1. Molecular structures of the Zn porphyrin photosensitizer (ZnF_{20}) and electron donors (DABCO and Asc).

To investigate the reductive quenching mechanism, 1,4-diazabicyclo[2.2.2]octane (DABCO, E_{ox} = 0.98 V vs. NHE)[28] and sodium ascorbate (Asc, E_{ox} = 0.69 V vs. NHE, Figure S2) are used as reversible electron donors (Figure 1) in acetonitrile (CH_3CN) and acetonitrile/water (CH_3CN/H_2O 6:4)solutions, respectively. The choice of these electron donors responds to their intrinsically different properties – DABCO, soluble in organic solvents, is known to coordinate to the metal center of the porphyrin,[29] whereas ascorbate can be used in water-containing mixtures,[30] which is desirable for artificial photosystems envisaging future practical applications.[31]

Experimental

Materials

DABCO, sodium ascorbate and acetonitrile are commercially available and were purchased from Sigma Aldrich. 1,3-dimethyl-2-phenyl-2,3-dihydro-1*H*benzo[*d*]imidazole (BIH) was prepared according to the literature.[32]

For the synthesis of ZnF_{20}, porphyrin-F_{20} ($C_{44}H_{10}F_{20}N_4$, 110 mg and 123 µmol) was dissolved in a 100 mL $CHCl_3$/MeOH 5:1 mixture. Then, $Zn(OAc)_2$ (207 mg, 1.23 mmol) and NaOAc (93 mg, 1.23 mmol) were added, and the reaction mixture was refluxed overnight. The reaction mixture was then filtered to remove the excess of salt and the solvent was evaporated under vacuum. The reaction crude was dissolved in 50 mL of $CHCl_3$ and 50 mL aqueous solution of 1 M $NaHCO_3$ was then added so the two phases were separated. The organic phase containing the final ZnF_{20} complex was filtered through a silica plug and evaporated under vacuum to obtain a purple powder in 90 % yield (105 mg).

Photoaccumulation and Spectroelectrochemistry

Photoaccumulation experiments were performed in a 1 cm quartz cuvette purged with Ar. A single beam SPECORD s600 spectrophotometer (Analytik Jena) was used to probe the UV-Vis absorption of the samples. Vigorous stirring conditions were maintained during a 405 nm (~58 mW) continuous laser excitation. Spectroelectrochemistry (SEC) experiments were performed in a quartz cuvette with a 1 mm optical path, with a Pt-mesh used as a working electrode, a Pt wire as a counter electrode and Ag/Ag^+ as a pseudo-reference. The chronoamperometry method was used to induce reduction.

Nanosecond Optical Transient Absorption Spectroscopy

The experimental setup used for optical transient absorption (OTA) measurements has been described in detail in previous reports.[10,11] Briefly, a tunable OPO laser set to 10 Hz is used as a pump and a supercontinuum white light laser operating at 20 Hz is used as an absorption probe. The pump-probe delays are electronically controlled as the differential spectra are obtained by subtracting the signals before and after the pump excitation.

Time-Resolved Resonance Raman Spectroscopy

Similarly, the time-resolved resonance Raman (TR3) experimental setup has been described elsewhere.[33] Two tunable OPO lasers are used as pump and probe, both operating at 20 Hz. The wavelength of the probe laser is adjusted to match electronic transitions of the photogenerated products thus ensuring the resonance conditions and the concomitant signal enhancement. UV-Vis absorption spectra of the sample are recorded before and after laser excitation experiments to ensure stability under the operational experimental conditions.

Computational Calculations

Fully unconstrained geometry optimizations have been carried out using the CAM-B3LYP functional as implemented in the Gaussian 16 package.[34] The Def2-TZVP basis set was applied to C, H, N, and F atoms. The inner electrons of Zn were treated with the effective core potential LANL2DZ[35] and the valence electrons with the associated double-ς basis set. The nature of all optimized geometries was confirmed through analysis of the harmonic vibrational frequencies at the same level of theory. Resonance Raman spectra were computed at the TD-DFT level of theory (CAM-B3LYP) using the aforementioned basis sets. The modified vibronic theory of Albrecht with the Independent Mode Displaced Harmonic Oscillator (IMDHO) model was employed.[33,36–38] The resulting theoretical resonance stick spectra were convoluted with Voigt functions (1:1, half-width 5 cm^{-1}) and normalized at the most intense mode. No scaling was applied to the resulting spectra.

Results and Discussion

The ability of DABCO to coordinate the porphyrin's metallic center in CH_3CN is the very first aspect to be considered in this system. With a binding constant in the order of 10^5-10^8 M^{-1},[39] this coordination has previously been described and built upon in the context of supramolecular self-assemblies[29,40–47]. Since the effect of DABCO's ligation can easily be observed in steady-state UV-Vis absorption spectra, we performed a titration of ZnF_{20} in the presence of the binding donor (Figure 2, top panel). Upon coordination, both the Soret and the Q-bands of ZnF_{20} are subject to a red shift of approximately 6 nm.

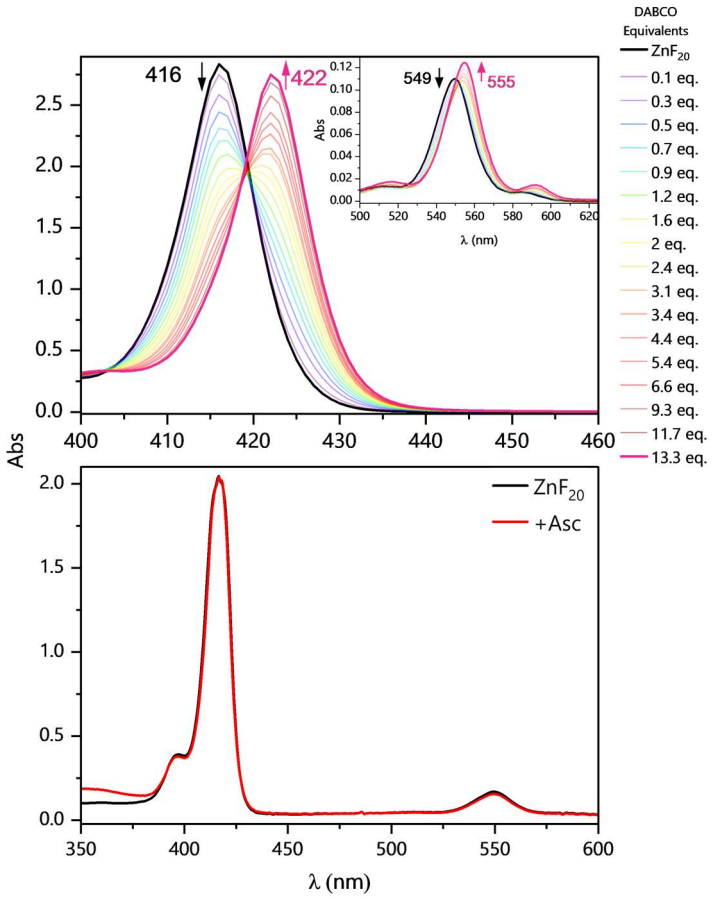

Figure 2. Absorption changes in the Soret band region and in the Q-bands (inset) upon titration of 4.9 μM ZnF_{20} with DABCO (top panel) in CH_3CN. Absorption spectrum of 4.9 μM ZnF_{20} in the absence and in the presence of 100 mM Asc (bottom panel) in CH_3CN/H_2O (6:4).

It is well known that, for micromolar-ranged concentrations of the porphyrin, a 1:1 complex with DABCO is formed, with further aggregation being possible under millimolar concentrations.[41] However, our titration dataset at micromolar concentration of ZnF_{20} reveals that a 1:1 and a 1:2 complex (ZnF_{20}-DABCO) are successively formed with equilibrium constants of K_{11} = 4.5 (± 1.3) ×10^5 M^{-1} and K_{12} = 1.7 (± 0.5) ×10^{10} M^{-1}, respectively (Figure S3). When Asc is used as an electron donor, no changes are observed in the absorption spectrum of ZnF_{20} (Figure 2, bottom panel) and so no relevant ground state interaction is expected to take place.

The same DABCO coordination effects can be observed in the emission spectra of ZnF_{20} in its initial Zn^{II} oxidation state (Figure S4) and in its chemically-prepared reduced form, hereafter formally denoted as Zn^{I} (Figure S5). For the chemical preparation of Zn^{I}, cobaltocene ($CoCp_2$) was used as a reducing agent (E_{red} = -0.96 V vs. NHE).[48] Since these particular behaviors of ZnF_{20} with different electron donors are likely to have implications on the dynamics of photoinduced charge separation, we set to look deeper into the this process through time-resolved spectroscopic approaches.

For OTA experiments, solutions of 5.8 μM of ZnF_{20} were consistently used and the porphyrin was excited at its Soret band (423 nm, 1 mJ/pulse). Excitaton of ZnF_{20} alone in CH_3CN shows the formation of its triplet state (denoted $^3Zn^*$) with a broad

excited state absorption (ESA) band centered at 453 nm (Figure 3a) and a monoexponential decay fitted with a time constant of 11.6 ± 0.2 µs (Figure S6). The same absorption signature was obtained in CH_3CN/H_2O (6:4) with a similar time constant of 26.0 ± 0.5 µs (Figure S7). In both cases, ~38±5% of the ground state population was converted into $^3Zn^*$. This estimation is based on the analysis of the bleaching Q-band with ε(553 nm) = ~20500 $M^{-1}cm^{-1}$ in CH_3CN.

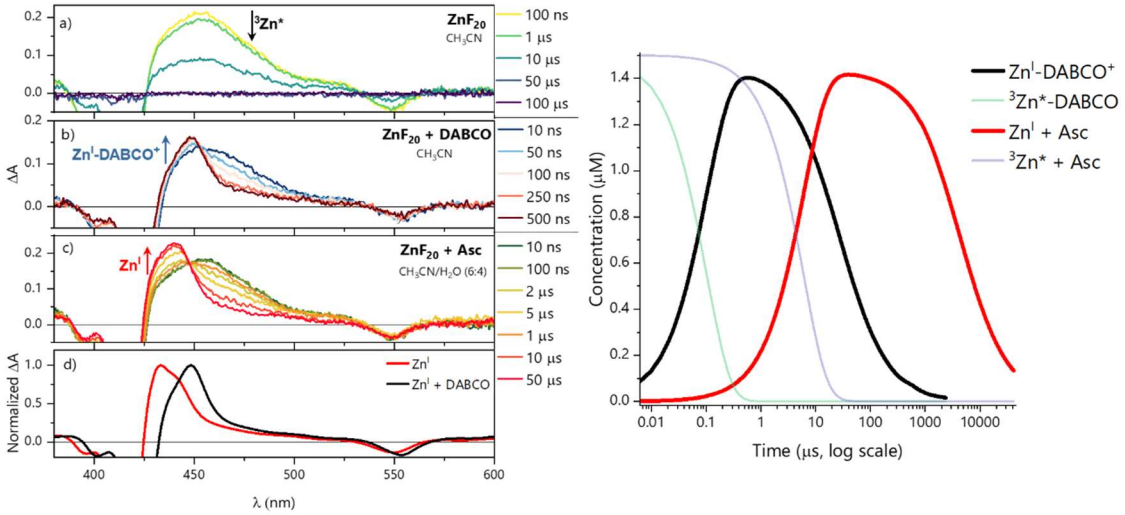

Figure 3. Transient absorption spectra (left panel) of a solution containing (a) 5.8 µM ZnF_{20} and upon addition of (b) 100 mM DABCO in CH_3CN or (c) ascorbate in CH_3CN/H_2O 6:4; (d) spectral references for Zn^I obtained via photoaccumulation experiments with BIH. Simulated concentration profiles (right panel) for the photogenerated species with both DABCO and Asc as electron donors. λ_{exc} = 423 nm, 1 mJ/pulse.

To investigate the reductive quenching mechanism, both DABCO and Asc were added in excess (100 mM) to samples containing 5.8 µM ZnF_{20}. The resulting absorption spectra are shown in Figure 2 (bottom) for ZnF_{20} + ascorbate and in Figure S8 for the DABCO-containing sample. Upon excitation, ~1.4 ± 0.4 µM of $^3Zn^*$ was created in both cases (Figure 3b and c). For DABCO, reductive quenching of the excited state is observed with the decay of $^3Zn^*$ at 453 nm as a new ESA band rises at 448 nm (Figure 3b). Simulations of the kinetic decays were carried out with the SKANA software[49] using bimolecular reactions of charge separation and recombination (Table S1). A quenching rate constant k_q = 9.2 (± 2.8) ×10^7 $M^{-1}s^{-1}$ was obtained as well as a high recombination constant k_{rec} = 2.6 (± 0.8) ×10^{10} $M^{-1}s^{-1}$ when DABCO was used as the electron donor. The charge separation efficiency was about 24 ± 3% with the formation of ~1.4 (± 0.4) µM Zn^I-DABCO$^+$.

In the case of ascorbate, the ESA band due to the formation of Zn^I appears blue-shifted with respect to DABCO, at 440 nm along with the decay of $^3Zn^*$ (Figure 3c and 3d). Kinetic simulations yielded slower quenching and recombination rate constants of k_q = 1.6 (± 0.5) ×10^6 $M^{-1}s^{-1}$ and k_{rec} = 1.8 (± 0.5) ×10^8 $M^{-1}s^{-1}$, respectively (Table S1). Again, a similar charge separation efficiency of ~26 ± 3% was observed. Details on the spectro-kinetic simulations are available in the Supporting Information (Table S1 and Figures S9-10). The formation of both Zn^I-DABCO$^+$ and Zn^I + ascorbate are confirmed by photoaccumulation (PA) experiments performed with 1,3-dimethyl-2-phenyl-2,3-

dihydro-1*H*benzo[*d*]imidazole (BIH) as a sacrificial nonbinding electron donor (Figure 3d and Figures S11-12) and by spectroelectrochemistry (SEC, Figures S13-14).

Although these systems have similar charge separation efficiency, their kinetics are intrinsically different. The right panel of Figure 3 shows the kinetic profiles of all photogenerated species when both DABCO and Asc are used as electron donors. In general, both the quenching and the charge recombination processes are much faster with DABCO compared to ascorbate. Indeed, this is directly manifested in the values of k_{rec} – the recombination takes place with a hundredfold increase in the order of magnitude for DABCO as compared to the ascorbate-containing sample (Table S1). We attribute this to the fact that DABCO axially binds to ZnF_{20}, forming a complex that behaves like a dyad with the charge separation and recombination processes having an intramolecular character in nature. On the other hand, with ascorbate, the same processes are completely driven by diffusion and longer-lived reduced states are generated.

We then tried to look deeper into the reductive quenching mechanism by probing vibrational changes in the Zn porphyrin. In order to perform time-resolved resonant Raman experiments, we set the laser pump to 554 nm (2.2 mJ/pulse) to excite ZnF_{20} at its Q-band and the laser probe was set to 447 nm (2.2 mJ/pulse), in resonance with the the T_1 excited state $^3Zn^*$ and the reduced state Zn^I of the porphyrin. For TR3, we increased the concentration to 12.6 μM ZnF_{20} due to the lower extinction coefficient at the Q-band.

We first investigated the formation of the triplet state by exciting the porphyrin alone. Pump excitation led to the formation and decay of new bands at 1655, 1528, 1283, 1223, and 774 cm^{-1} (Figure 4). Similar bands of the triplet excited state have been previously identified for ZnTPP[50] under similar Soret resonance conditions. The assignments of these bands have been discussed in the literature,[50,51] and they are available in Table 1 together with the corresponding calculated DFT frequencies. It is noteworthy that, with respect to ZnTPP, the presence of perfluorinated phenyl rings in ZnF_{20} causes frequency shifts due to increased force constants, specially on the modes with a strong phenyl character, such as the one observed at 1655 cm^{-1} (Figure S15). Other modes are also strongly affected by fluorination. The corresponding theoretical spectra for the ground and excited states under resonance conditions are available in Figure S16.

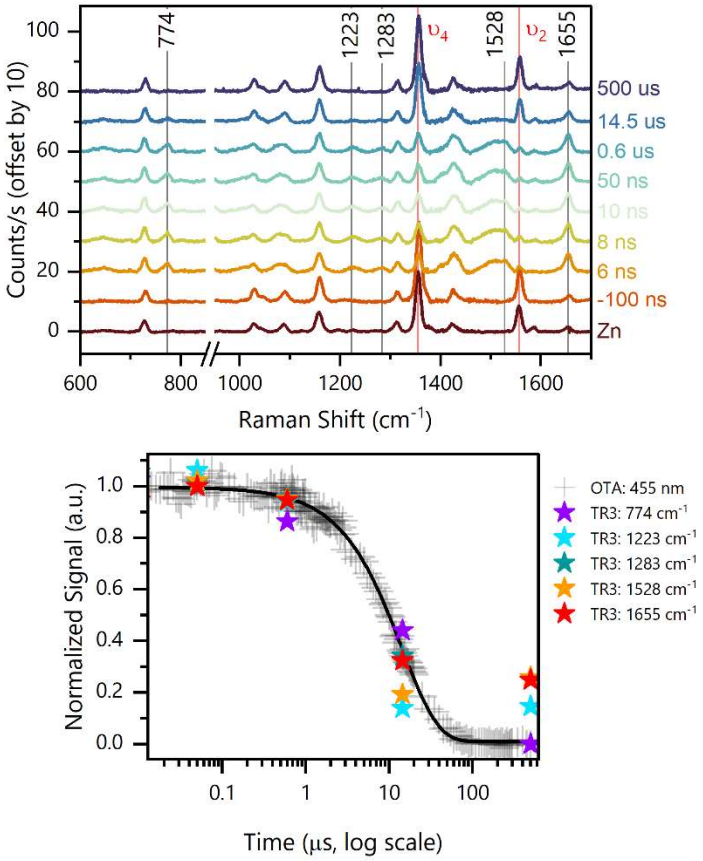

Figure 4. TR3 spectra (top panel) obtained upon exciting 12.6 μM ZnF_{20} in CH_3CN. Solid vertical lines represent time-evolving bands due to the formation of $^3Zn^*$. Overlapped kinetic decays (bottom panel) obtained by OTA and TR3 under the same experimental conditions. λ_{pump} = 554 nm, 2.2 mJ/pulse; λ_{probe} = 447 nm, 2.2 mJ/pulse.

Interestingly, the ν_2 mode observed at 1559 cm^{-1} for ZnF_{20} in its ground state (solid red line in Figure 4) exhibits a strong time-dependent decrease in intensity upon formation of the triplet state (-100 ns to 0.6 μs) concomitant with the rise of a new band at 1528 cm^{-1}. This indicates that this mode is strongly spin-state-sensitive as in the case for iron-based porphyrins.[52] In fact, a similar downshift of 40 cm^{-1} has been previously demonstrated upon populating the triplet state of ZnTPP.[50] Although a weaker intensity loss was observed in the ν_4 mode at 1357 cm^{-1}, it did not exhibit any shift in frequency.

In addition, we observed a new band of $^3Zn^*$ at 774 cm^{-1} which according to our DFT calculations can be assigned to ν_{16}. This feature presents a strong component of the δ(CαNCα) mode and a strong phenyl contribution, having previously been described as symmetric pyrrole deformation in the metalloporphyrin D_{4h}-core.[53] Finally, we show (Figure 4, bottom panel) that all detected TR3 vibrations follow the same kinetics as the ESA band of $^3Zn^*$, further corroborating their nature.

We then investigated the reductive quenching mechanism in the presence of both electron donors. Since no differences are observed in the resonant Raman spectra in the presence of either DABCO or ascorbate (Figure S17), as additionally shown by our DFT calculations (Figure S18), only the results related to the DABCO-containing system will be discussed. Excitation of 12.6 μM ZnF_{20} in the presence of

100 mM DABCO in CH_3CN led to the time-resolved evolution of new bands detected at 636, 1277, and 1540 cm^{-1} (Figure 5, left panel). The reference spectrum of the chemically prepared Zn^I species in the presence of 100 mM DABCO is displayed in Figure S19, together with the corresponding theoretical resonance Raman spectrum of Zn^I shown in Figure S20.

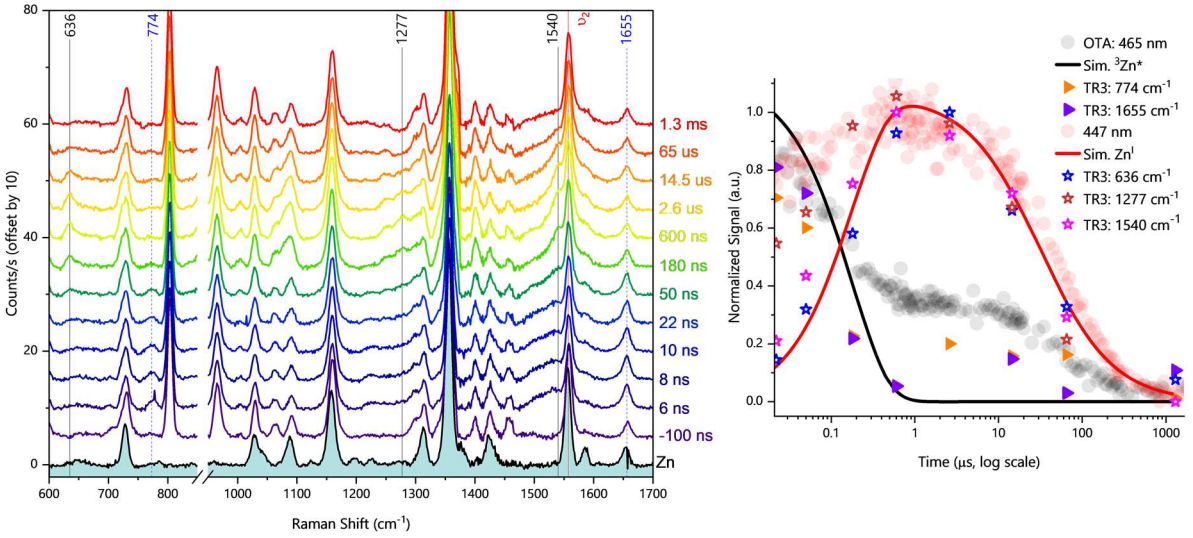

Figure 5. TR3 spectra (left panel) obtained upon exciting 12.6 µM ZnF_{20} in the presence of 100 mM DABCO in CH_3CN. Black solid lines represent time-evolving bands due to the formation of Zn^I and dashed blue lines indicated the bands of $^3Zn^*$. Overlapped kinetic decays (right panel) obtained by OTA and TR3 under the same experimental conditions, with solid lines showing the simulated evolution of relevant photogenerated species. λ_{pump} = 554 nm, 2.2 mJ/pulse; λ_{probe} = 447 nm, 2.2 mJ/pulse.

Once again, we observed a downshift of 19 cm^{-1} in the ν_2 mode detected, this time, at 1540 cm^{-1}. This indicates that, in addition to being spin-state-sensitive, this mode is also sensitive to the oxidation state of the Zn-porphyrin. As a consequence of these two features, this mode constitutes an excellent probe for photochemical processes involving ZnF_{20} as a photosensitizer. The downshift of this band, due to the formation of both the triplet and reduced states, can be explained by the population of the LUMO orbital of the porphyrin macrocycle, weakening the π bonds of the conjugated rings.[50]

The mode at 1277 cm^{-1} has also been previously observed and assigned to the reduced state of ZnTPP in previous studies,[54,55] and it has been identified as $\nu(C_m\text{-}C_{ph})$. Our calculations are in agreement with this assignment for ZnF_{20} and, because this mode is of totally symmetric nature,[54] it can be attributed to ν_1.[53] Finally, we have detected a new band at 636 cm^{-1}, also predicted by our DFT calculations, assigned to an out-of-plane phenyl vibration involving the fluorine atoms. A similar phenyl mode has been observed for NiTPP and it can be tentatively assigned to π_3', a mode described by a γ(CH) component in the hydrogenated phenyl ring that, naturally, becomes γ(CF) for ZnF_{20} (Figure S21).

Table 1. Vibrational frequencies (in cm^{-1}) of the main peaks observed in TR3 experiments attributed to ZnF_{20}, $^3Zn^*$ and Zn^I.

ZnF_{20}			$^3Zn^*$			Zn^I			
Exp.	DFT[a]	Lit.[b]	Exp.	DFT[a]	Lit.[b]	Exp.	DFT[a]	Lit.[b]	Assignment[c]
1656	1714	1598[50]	1655	1714	1596[50]				Φ_4 (phenyl)
1559	1632	1548[50]	1528	1618	1508[50]	1540	1554	1532[50]	ν_2, $\nu(C_\alpha\text{-}C_m)$
1357	1412	1352[50]							ν_4, $\nu(C_\alpha\text{-}N)$
1313	1353	1302[53]							ν_{12}, $\nu(C_\alpha\text{-}N)$
			1283	1302	1287[50]	1277	1282	1257[50]	ν_{27}, $\nu(C_m\text{-}C_{ph})$
			1223	1285	1233[50]				ν_1, $\nu(C_m\text{-}C_{ph})$
1158	1188	1179[50]							Φ_6 (phenyl)
730	752	639							Φ_9 (phenyl)?
			774	801	846[53]				ν_{16}, $\delta(\text{pyr def})_{sym}$
						636	672		π_3', γ(CF)

[a]Unscaled vibrational frequencies obtained from our CAM-B3LYP/Def2-TZVP/LANL2DZ calculations. [b]Literature values observed either for ZnTPP[50] or NiTPP[53]. [c]Assignments of relevant vibrational modes according to the metalloporphyrin core classification and the numbering scheme commonly used in the literature.[53]

Remarkably, the time evolutions of the three reduced state bands of ZnF_{20} follow the same kinetics observed for the 447 nm band in OTA experiments (Figure 5, right panel). Not only the reduced state bands are visible in the presence of DABCO, but the excited state bands at 774 cm^{-1} and 1655 cm^{-1} are also present and are likewise shown to evolve with the same kinetics observed under the same conditions in OTA. Indeed, these results illustrate the complementarity of these two experimental approaches to track the fate of transient species through the lenses of different probing strategies, thus providing valuable information on the nature and dynamics of molecular photosystems.

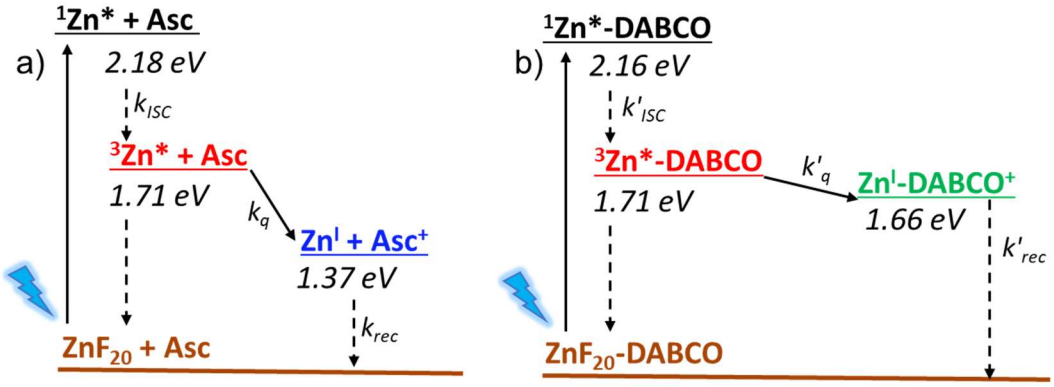

Figure 6. Jablonsky energy level diagram and reaction pathways for ZnF_{20} in the presence of a) ascorbate, and b) DABCO as reversible electron donors. k_q = 1.6 (± 0.5) ×10^6 $M^{-1}s^{-1}$, k_{rec} = 1.8 (± 0.5) x10^8 $M^{-1}s^{-1}$, k'_q = 9.2 (± 2.8) ×10^7 $M^{-1}s^{-1}$, k'_{rec} = 2.6 (± 0.8) ×10^{10} $M^{-1}s^{-1}$.

Lastly, we investigated the charge separation thermodynamics in both DABCO and ascorbate-containing systems. The energy level diagrams with the reaction pathways of all relevant photoinduced processes are presented in Figure 6. It should be noted that the energy of $^3Zn^*$ (~1.71 eV) was estimated from the phosphorescence spectrum recorded in an ethanol/methanol solvent mixture at 77 K (Figure S22).

Because the energy of the first excited singlet state (^{1}Zn*-DABCO) is virtually unaffected by the presence of DABCO, we assume that its effect is also negligible for the lowest lying triplet state (^{3}Zn*-DABCO). The energy level diagram of Figure 6 makes it evident that DABCO provides an electron transfer driving force that is 290 mV lower than that of ascorbate. Despite this, efficient reductive quenching of the excited state is observed with DABCO, with faster reaction rates of electron transfer and recombination that are likely associated to its coordination to the metal center.

Conclusions

Although the systems containing ZnF_{20} and DABCO/ascorbate have similar charge separation efficiencies, they display intrinsically different kinetic properties exhibiting much faster quenching and charge recombination reaction rates with DABCO. Indeed, the estimated rate constants with DABCO are more compatible with intramolecular electron transfer processes as compared to ascorbate-containing samples. In the latter, the same processes are clearly governed by diffusion and so the charge-separated state has a much longer lifetime. This prolonged lifetime increases its probability of engaging in bimolecular electron transfer reactions with other molecular species, such as specialized catalysts. Overall, we provide a complete photophysical characterization of ZnF_{20} in reductive quenching reaction mechanisms using complementary time-resolved techniques to generate and probe transient charge-separated states. Such studies contribute to the very fundamental understanding of primordial light-induced processes operating in artificial photosynthetic systems.

References

1 V. Balzani, A. Credi and M. Venturi, *Photochemical conversion of solar energy*, 2008, vol. 1.
2 D. Gust, T. A. Moore and A. L. Moore, *Acc. Chem. Res.*, 2009, **42**, 1890–1898.
3 J. W. Wang, D. C. Zhong and T. B. Lu, *Coord. Chem. Rev.*, 2018, **377**, 225–236.
4 B. Zhang and L. Sun, *Chem. Soc. Rev.*, 2019, **48**, 2216–2264.
5 C. Herrero, A. Quaranta, W. Leibl, A. W. Rutherford and A. Aukauloo, *Energy Environ. Sci.*, 2011, **4**, 2353–2365.
6 E. Romero, V. I. Novoderezhkin and R. Van Grondelle, *Nature*, 2017, **543**, 355–365.
7 M. H. Ha-Thi, V. T. Pham, T. Pino, V. Maslova, A. Quaranta, C. Lefumeux, W. Leibl and A. Aukauloo, *Photochem. Photobiol. Sci.*, 2018, **17**, 903–909.
8 M. Kuss-Petermann and O. S. Wenger, *Helv. Chim. Acta*, 2017, **100**, 1–7.
9 M. Kuss-Petermann, M. Orazietti, M. Neuburger, P. Hamm and O. S. Wenger, *J. Am. Chem. Soc.*, 2017, **139**, 5225–5232.
10 T. T. Tran, T. Pino and M. H. Ha-Thi, *J. Phys. Chem. C*, 2019, **123**, 28651–28658.
11 T. T. Tran, M. H. Ha-Thi, T. Pino, A. Quaranta, C. Lefumeux, W. Leibl and A. Aukauloo, *J. Phys. Chem. Lett.*, 2018, **9**, 1086–1091.
12 J. G. Vos and J. M. Kelly, *Dalt. Trans.*, 2006, 4869–4883.
13 F. E. Poynton, S. A. Bright, S. Blasco, D. C. Williams, J. M. Kelly and T. Gunnlaugsson, *Chem. Soc. Rev.*, 2017, **46**, 7706–7756.
14 F. Heinemann, J. Karges and G. Gasser, *Acc. Chem. Res.*, 2017, **50**, 2727–2736.
15 D. M. Arias-Rotondo and J. K. McCusker, *Chem. Soc. Rev.*, 2016, **45**, 5803–5820.
16 P. Herr, C. Kerzig, C. B. Larsen, D. Häussinger and O. S. Wenger, *Nat. Chem.*, 2021, **13**, 956–962.
17 C. D. Windle, M. W. George, R. N. Perutz, P. A. Summers, X. Z. Sun and A. C. Whitwood, *Chem. Sci.*, 2015, **6**, 6847–6864.
18 T. Gatti, P. Cavigli, E. Zangrando, E. Iengo, C. Chiorboli and M. T. Indelli, *Inorg. Chem.*, 2013, **52**, 3190–3197.
19 D. Il Won, J. S. Lee, Q. Ba, Y. J. Cho, H. Y. Cheong, S. Choi, C. H. Kim, H. J. Son, C. Pac and S. O. Kang, *ACS Catal.*, 2018, **8**, 1018–1030.
20 M. Andersson, J. Davidsson, L. Hammarström, J. Korppi-Tommola and T. Peltola, *J. Phys. Chem. B*, 1999, **103**, 3258–3262.
21 J. Petersson, M. Eklund, J. Davidsson and L. Hammarström, *J. Phys. Chem. B*, 2010, **114**, 14329–14338.
22 K. Kiyosawa, N. Shiraishi, T. Shimada, D. Masui, H. Tachibana, S. Takagi, O. Ishitani, D. A. Tryk and H. Inoue, *J. Phys. Chem. C*, 2009, **113**, 11667–11673.
23 Yong Hee Kim, Dae Hong Jeong, D. Kim, Sae Chae Jeoung, Hyun Sun Cho, Seong Keun Kim, N. Aratani and A. Osuka, *J. Am. Chem. Soc.*, 2001, **123**, 76–86.
24 I. W. Hwang, H. S. Cho, D. H. Jeong, D. Kim, A. Tsuda, T. Nakamura and A. Osuka, *J. Phys. Chem. B*, 2003, **107**, 9977–9988.
25 P. Osswald, C. C. You, V. Stepanenko and F. Würthner, *Chem. - A Eur. J.*, 2010, **16**, 2386–2390.
26 S. S. Nurttila, R. Becker, J. Hessels, S. Woutersen and J. N. H. Reek, *Chem. - A Eur. J.*, 2018, **24**, 16395–16406.
27 Y. Wu, J. Jiang, Z. Weng, M. Wang, D. L. J. Broere, Y. Zhong, G. W. Brudvig, Z. Feng and H. Wang, *ACS Cent. Sci.*, 2017, **3**, 847–852.
28 M. Jonsson, A. Houmam, G. Jocys and D. D. M. Wayner, *J. Chem. Soc. Perkin Trans. 2*, 1999, 425–429.
29 C. C. Mak, N. Bampos and J. K. M. Sanders, *Angew. Chemie - Int. Ed.*, 1998, **37**, 3020–3023.
30 Y. Pellegrin and F. Odobel, *Comptes Rendus Chim.*, 2017, **20**, 283–295.
31 Y. Yamazaki, H. Takeda and O. Ishitani, *J. Photochem. Photobiol. C*, 2015, **25**, 106–137.

32 E. Hasegawa, T. Seida, N. Chiba and C. Hart, *J. Org. Chem.*, 2005, **70**, 9632–9635.
33 D. H. Cruz Neto, J. Soto, N. Maity, C. Lefumeux, T. Nguyen, P. Pernot, K. Steenkeste, D. Peláez, M. H. Ha-Thi and T. Pino, *J. Phys. Chem. Lett.*, 2023, **14**, 4789–4795.
34 M. J. Frisch, G. W. Trucks, H. B. Schlegel, G. E. Scuseria, M. a. Robb, J. R. Cheeseman, G. Scalmani, V. Barone, G. a. Petersson, H. Nakatsuji, X. Li, M. Caricato, a. V. Marenich, J. Bloino, B. G. Janesko, R. Gomperts, B. Mennucci, H. P. Hratchian, J. V. Ortiz, a. F. Izmaylov, J. L. Sonnenberg, Williams, F. Ding, F. Lipparini, F. Egidi, J. Goings, B. Peng, A. Petrone, T. Henderson, D. Ranasinghe, V. G. Zakrzewski, J. Gao, N. Rega, G. Zheng, W. Liang, M. Hada, M. Ehara, K. Toyota, R. Fukuda, J. Hasegawa, M. Ishida, T. Nakajima, Y. Honda, O. Kitao, H. Nakai, T. Vreven, K. Throssell, J. a. Montgomery Jr., J. E. Peralta, F. Ogliaro, M. J. Bearpark, J. J. Heyd, E. N. Brothers, K. N. Kudin, V. N. Staroverov, T. a. Keith, R. Kobayashi, J. Normand, K. Raghavachari, a. P. Rendell, J. C. Burant, S. S. Iyengar, J. Tomasi, M. Cossi, J. M. Millam, M. Klene, C. Adamo, R. Cammi, J. W. Ochterski, R. L. Martin, K. Morokuma, O. Farkas, J. B. Foresman and D. J. Fox, 2016.
35 P. J. Hay and W. R. Wadt, 1985, **82**, 299–310.
36 D. Aranda, F. J. Avila, I. López-Tocón, J. F. Arenas, J. C. Otero and J. Soto, *Phys. Chem. Chem. Phys.*, 2018, **20**, 7764–7771.
37 M. R. Lopez-Ramirez, D. Aranda Ruiz, F. J. Avila Ferrer, S. P. Centeno, J. F. Arenas, J. C. Otero and J. Soto, *J. Phys. Chem. C*, 2016, **120**, 19322–19328.
38 J. Soto, E. Imbarack, I. López-Tocón, S. Sánchez-Cortés, J. C. Otero and P. Leyton, *RSC Adv.*, 2019, **9**, 14511–14519.
39 H. W. Wang, C. H. Chen, T. S. Lim, S. L. Huang and T. Y. Luh, *Chem. - An Asian J.*, 2011, **6**, 524–533.
40 H. L. Anderson, C. A. Hunter, M. Nafees Meah and J. K. M. Sanders, *J. Am. Chem. Soc.*, 1990, **112**, 5780–5789.
41 L. Baldini, P. Ballester, A. Casnati, R. M. Gomila, C. A. Hunter, F. Sansone and R. Ungaro, *J. Am. Chem. Soc.*, 2003, **125**, 14181–14189.
42 M. C. Lensen, S. J. T. Van Dingenen, J. A. A. W. Elemans, H. P. Dijkstra, G. P. M. Van Klink, G. Van Koten, J. W. Gerritsen, S. Speller, R. J. M. Nolte and A. E. Rowan, *Chem. Commun.*, 2004, **4**, 762–763.
43 D. I. Schuster, K. Li, D. M. Guldi and J. Ramey, *Org. Lett.*, 2004, **6**, 1919–1922.
44 P. Ballester, A. I. Oliva, A. Costa, P. M. Deyà, A. Frontera, R. M. Gomila and C. A. Hunter, *J. Am. Chem. Soc.*, 2006, **128**, 5560–5569.
45 S. Hecht and J. M. J. Fréchet, *Angew. Chemie - Int. Ed.*, 2001, **40**, 74–91.
46 T. Ishida, Y. Morisaki and Y. Chujo, *Tetrahedron Lett.*, 2006, **47**, 5265–5268.
47 T. Kishida, N. Fujita, O. Hirata and S. Shinkai, *Org. Biomol. Chem.*, 2006, **4**, 1902–1909.
48 A. Badalyan, Z. Y. Yang and L. C. Seefeldt, *ACS Catal.*, 2019, **9**, 1366–1372.
49 P. Pernot, .
50 R. A. Reed, R. Purrello, K. Prendergast and T. G. Spiro, *J. Phys. Chem.*, 1991, **95**, 9720–9727.
51 V. A. Walters, J. C. De Paula, G. T. Babcock and G. E. Leroi, *J. Am. Chem. Soc.*, 1989, **111**, 8300–8302.
52 C. Römelt, S. Ye, E. Bill, T. Weyhermüller, M. Van Gastel and F. Neese, *Inorg. Chem.*, 2018, **57**, 2141–2148.
53 X. Y. Li, R. S. Czernuszewicz, J. R. Kincaid, Y. O. Su and T. G. Spiro, *J. Phys. Chem.*, 1990, **94**, 31–47.
54 M. Atamiaiv, R. J. Donohoe and D. F. Bocian, 1989, 2236–2243.
55 H. Yamaguchi, A. Soeta, H. Toeda and K. Itoh, *J. Electroanal. Chem.*, 1983, **159**, 347–359.